A Frequency Independent Closed-Loop Frequency Dithering Technique to Attenuate Conducted EMI for Dual-Active Bridge Series Resonant Converter

Kousik Ghosh, *Student Member, IEEE*, Vibhav Pandey, *Student Member, IEEE*, and Kamalesh Hatua, *Member, IEEE*

***Abstract*—The frequency dithering techniques (FDT) to attenuate electromagnetic interference (EMI) are widely researched in the literature. However, the existing FDTs cannot be applied to resonant converters, where state and output variables are functions of switching frequency. This article proposes an FDT combined with frequency-independent closed-loop control for dual-active bridge series resonant converters (DABSRC). The proposed combined technique attenuates the EMI noise and simultaneously regulates the output variables, making it independent of switching frequency variation. The FDT considers five switching frequencies from 66 to 72 kHz in steps of 1.5 kHz. The proposed FDT considers the effect of resolution bandwidth (RBW) of 9 kHz as per EMI standards, which is largely neglected in the literature. The frequency dependence of the output variables is eliminated by a modified large-signal model-based control (MLSMC) through feedforward cancellation. The proposed technique achieves a significant EMI attenuation of 8 dB along with decoupled output voltage and reactive power control. This achieves a filter size reduction by 34% . In addition, the settling time achieved for output voltage and reactive power is 5 ms for a load transition of as high as 62.5% . The results are experimentally validated on a 1.5 kW DABSRC prototype.**

***Index Terms*—Dual-active bridge series resonant converters (DABSRC), electromagnetic interference (EMI) attenuation, EMI, frequency dithering technique (FDT), frequency independent control, resolution bandwidth (RBW).**

I. Introduction

THE advancements in semiconductor technology have led to the use of wide-bandgap (WBG) devices in power electronic converters. This has increased the power density because of higher switching frequency and fast switching [1]. The applications include microgrids [2], electric vehicle [3], solid-state transformers [4], etc. Dual-active bridge series resonant converter (DABSRC) is one of the most widely used topologies in these applications because of its simpler topology, wider soft-switching and dc blocking capability. However, using WBG devices generates electromagnetic compatibility issues because of high switching frequency and fast voltage and current transitions [5]. The electromagnetic interference (EMI) noise arising from the device switching causes voltage and current oscillations of the input supply if not suppressed adequately [6]. The conducted EMI is divided into differential mode (DM) and common mode (CM) noise, which need to pass the standards defined in CISPR-11 [7] by the International Electrotechnical Commission for industrial applications.

The EMI attenuation is largely achieved through EMI filters, which are classified into active and passive filters. The passive filters conversely reduce the power density, as they consist of bulky inductors [8]. The active filters require additional circuits, which make them complex to implement and bulky as well [9].

In order to reduce the size of the EMI filters, one of the widely used techniques in literature is the frequency dithering or spread spectrum technique. In the case of a single switching frequency operation, the total energy is concentrated on the same frequency. Whereas, the frequency dithering technique (FDT) spreads the energy of one frequency over a range of frequencies, reducing the effective magnitude in the conducted EMI zone. Various FDT have been highlighted in [10], [11], [12], and [13]. These techniques do not consider the effect of resolution bandwidth (RBW) of 9 kHz for EMI measurement, which is specified by the CISPR-11 standard [7]. RBW is the bandwidth of a bandpass filter that applies to the input signal of the spectrum analyzer. It measures the resultant magnitude of all the frequency components within an RBW window. A random dithering technique for buck converter has been proposed in [10], which randomly selects the switching frequencies, achieving 6 dB reduction. The periodic dithering technique in [11] varies over 20 switching frequencies uniformly to achieve 20 dB attenuation. However, the abovementioned frequency dithering methods do not consider the RBW of 9 kHz, which violates the CISPR-11 standard. The dithering technique in [12] and [13] considers five and seven discrete switching frequencies in steps of 3 kHz achieving 4 and 7 dB attenuation, respectively. These techniques have a very wide frequency variation due to the large frequency hop. All the abovementioned dithering techniques have been implemented in converters, where output variables are independent of switching frequency. However, the same is not applicable for resonant converters, where the output variable is a function of switching frequency. This makes the output variables vary continuously with frequency variation. In

Received 6 March 2025; revised 23 July 2025; accepted 22 August 2025. Date of publication 25 August 2025; date of current version 22 October 2025. Recommended for publication by Associate Editor H. Li. *(Corresponding author: Kousik Ghosh.)*

The authors are with the Department of Electrical Engineering, IIT Madras, Chennai 600036, India (e-mail: ee21d750@smail.iitm.ac.in; ee18d421@smail.iitm.ac.in; kamalesh@ee.iitm.ac.in).

Color versions of one or more figures in this article are available at https://doi.org/10.1109/TPEL.2025.3602518.

Digital Object Identifier 10.1109/TPEL.2025.3602518

addition, the high dithering frequency interferes with controller bandwidth. Thus, a specialized control technique to regulate the output variables, along with the FDT, is required. A periodic triangular frequency modulation is used for the *LLC* resonant converter combined with phase-shift control in [14], [15], [16], and [17] to regulate the output voltage. A 16 dB attenuation is achieved in [14] with hybrid pulsewidth modulation control and triangular frequency dithering over 14 kHz frequency variation. In [15], pulse-frequency control along with triangular frequency modulation over 13.5 kHz achieves 12 dB attenuation. A hybrid control algorithm with a frequency variation range of 24 kHz achieves 22 dB attenuation in a current-fed *LLC* converter [16]. The partial power processing concept with spread-spectrum in half-bridge *LLC* converter [17] achieves 25 dB attenuation with 80 kHz frequency variation. A similar improved phase-shift control-based FDT for DAB is reported in [18], which achieves 12 dB attenuation with 10 kHz frequency variation. FDT with a second harmonic ripple-based control for *LLC* is implemented in [19] and achieves 17 dB attenuation. All the abovementioned methods do not consider the mandated RBW violating CISPR-11 standard and exhibit only single-variable control, which increases losses. Pulsewidth modulation control for *CLLC* converter in [20] considers 9 kHz RBW but achieves only 4 dB attenuation with single-variable control.

The reported control methods of DABSRC are either for fixed frequency control or utilize switching frequency as a control variable. The linearized control techniques in [21], [22], and [23], and the model-predictive nonlinear control in [24], [25], and [26] are all dependent on switching frequency. Thus, the frequency dithering causes the respective control governing equations to change continuously, making the control unstable for frequency dithering. This will cause a large ripple in output variables at steady state. Similarly, the large-signal control in [27] is applicable for fixed frequency control. As the large-signal variables cannot be generated with varying switching frequency. Thus, the objectives to attenuate EMI in DABSRC are as follows.

1) To maximize the achievable EMI attenuation considering 9 kHz RBW.
2) To develop a switching frequency independent multivariable control method.

This article presents an FDT considering five switching frequencies with frequency steps of 1.5 kHz from 66 to 72 kHz. The switching frequencies and dithering frequency are selected to maximize the achieved attenuation considering 9 kHz RBW, which has been largely neglected in the literature. Also, the persisting time of each switching frequency is selected to eliminate the effect of frequency dithering on controller bandwidth. In addition, a multivariable modified large-signal model-based control (MLSMC) has been proposed in this article to nullify the effect of frequency dithering in the output variables, which has not been attempted in the literature. The simplified control technique MLSMC achieves decoupled multivariable control of output voltage and reactive power (minimum rms current) control of DABSRC. The large-signal transfer functions are made independent of switching frequency by the feedforward cancellation, making it constant throughout the frequency variation

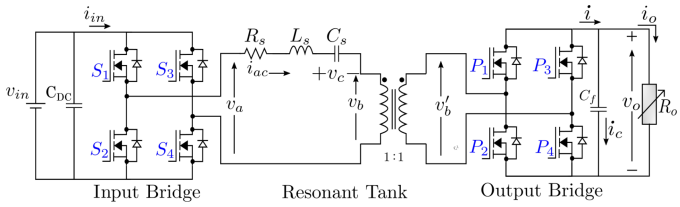

Fig. 1. Schematic of a DABSRC.

range. The feedforward cancellation also decouples active and reactive powers. The control technique estimates active and reactive components of the state variables independent of switching frequency. The proposed FDT combined with MLSMC achieves an EMI noise reduction of around 8 dB, along with decoupled constant voltage and reactive power control. This technique eliminates the DM filter and reduces the CM filter volume by 34% . Moreover, the settling time achieved for output voltage and reactive power is 5 ms subjected to load transition of as high as 62.5% . The experimental validations are performed on a 1.5 kW DABSRC hardware prototype.

The rest of the article is organized as follows. Section II highlights the existing and proposed solution. Section III presents the proposed dithering algorithm. Section IV describes the control algorithm. Section V shows the experimental results. Section VI presents the performance comparison. Finally, Section VII concludes the article.

II. Existing and Proposed Solution

The DABSRC shown in Fig. 1 draws the input current (i_{in}) having average and harmonic components from a dc source (v_{in}). The ripple component arises because of the switching of the SiC-MOSFETs in DABSRC. This ripple component of the current consists of the switching frequency and its harmonics, whose magnitudes are manifested as the EMI noise. The input current is drawn through a line impedance stabilization network (LISN) connected after the dc source to measure the EMI noise.

A. Existing Solution

The various FDT are reported in [10], [11], [12], [13], [14], [15], [16], [17], [18], and [19]. However, the abovereported dithering techniques do not consider the 9 kHz RBW mandated by CISPR-11 and the effect of sidebands due to FDT. Also, for DABSRC, a control technique is needed to eliminate the effect of frequency dithering on output variables. Various control techniques for frequency dithering in [14], [15], [16], [17], [18], [19], and [20] are reported for resonant converter. However, these techniques do not implement the reactive power control along with output voltage, which increases losses [21], [27]. In the case of the existing multivariable control techniques, the plant transfer function in linearized control [21], [22], [23] is a function of switching frequency. Thus, with frequency dithering, the nature of the plant transfer functions varies continuously. As a result, the designed gain crossover frequency (GCF) of the control loop will also vary. Hence, a controller designed for a particular switching frequency cannot control the output

variables with frequency dithering. Similarly, the plant model for nonlinear control [24], [25], [26] also depends on frequency. Thus, the optimization and cost functions minimization blocks in nonlinear control designed for a particular plant model cannot predict the correct solutions in case of frequency dithering as the governing equations keep varying. The large-signal control in [27] cannot estimate the active and reactive power components for variable frequency. As a result, in all cases, the controller cannot eliminate the steady-state error, giving rise to a large ripple in output variables.

This requires a frequency-independent control technique to implement frequency dithering in DABSRC, complying with CISPR-11 standards.

B. Proposed Solution

The proposed FDT, combined with the frequency-independent control, considers the effect of frequency dithering on the output variables of DABSRC. It also considers the CISPR-mandated 9 kHz RBW. The switching frequencies and the dithering frequency are selected to minimize the number of switching frequencies or its harmonic components within an RBW window. The simplified technique MLSMC is developed to control active and reactive power simultaneously independent of switching frequency. Active power control regulates the output voltage, while reactive power control ensures minimum rms current. This necessitates two equivalent control loops and circuit models separately for active and reactive power. The transfer functions of the control loops are made independent of switching frequency using the feedforward cancellation. This makes the plant transfer functions constant and dependent only on circuit parameters. Thus, the designed GCF of the loop transfer function is also fixed throughout the operating frequency range. The feedforward and feedback terms in the control loop are constituted by the active and reactive components of the state variables, which are estimated independent of the switching frequency. The estimation is carried out in the analogue domain to eliminate high-frequency analog to digital coverters (ADCs).

The required detailed frequency dithering algorithm followed by the control algorithm and estimation of active–reactive components independent of switching frequency are explained in the next sections.

III. Frequency Dithering Technique

The first step includes modeling the input current of DABSRC for frequency dithering and investigating the frequency components arising from that. Thereafter, the switching frequency, dithering frequency, and persisting times of each switching frequency or dithering duty are calculated to maximize the achieved EMI attenuation.

A. Modeling of EMI in DABSRC

The input current ($i_{\text{in}}(t)$) of DABSRC, which gives rise to EMI, is a rectified phase-shifted sinusoidal current, which can be expressed as

$$i_{\text{in}}(t) = \begin{cases} I_{\text{pk}} \sin(\omega_s t - \phi_i), & 0 < \omega_s t < \pi \\ -I_{\text{pk}} \sin(\omega_s t - \phi_i), & \pi < \omega_s t < 2\pi \end{cases} \tag{1}$$

where I_{pk} is the peak magnitude of i_{ac}, ω_s is the switching frequency, and ϕ_i is the phase-angle between the ac-link current (i_{ac}) and input-bridge voltage (v_a). Now, in the case of minimum rms current or reactive power control, i_{ac} comes in the same phase with v_a, making $\phi_i = 0^o$. Also, ϕ_i affects only the phase and not the magnitude of i_{in}. Hence, it does not affect the EMI attenuation. The frequency components in $i_{\text{in}}(t)$ with and without frequency dithering are derived hereafter.

1) Without Frequency Dithering: Considering the general form of $i_{\text{in}}(t)$ in (1), $i_{\text{in}}(t)$ can also be expressed as $i_{\text{in}}(t) = S(t) I_{\text{pk}} \sin \omega_s t$, where $S(t)$ is the rectifying function and can be expressed as

$$S(t) = \begin{cases} 1, & 0 < \omega_s t < \pi \\ -1, & \pi < \omega_s t < 2\pi. \end{cases} \tag{2}$$

The frequency components of $i_{\text{in}}(t)$ can be obtained through Fourier analysis and can be expressed as

$$\begin{aligned} i_{\text{in}} &= I_{\text{pk}} \sum_{n=1,3,5}^{\infty} \frac{4}{n\pi} \sin n\omega_s t \sin \omega_s t \\ &= \frac{2I_{\text{pk}}}{\pi} \sum_{n=1,3,5}^{\infty} \frac{1}{n} \{\cos(n-1)\omega_s t - \cos(n+1)\omega_s t\} \\ &= \frac{2I_{\text{pk}}}{\pi} - \frac{4I_{\text{pk}}}{\pi} \sum_{n=2,4,6}^{\infty} \frac{1}{n^2-1} \cos(n\omega_s t). \end{aligned} \tag{3}$$

Thus, it can be inferred from (3) that the frequency components will be at $n\omega_s$, where $n = 2, 4, 6, \ldots$ is the even harmonic order of switching frequency.

2) With Frequency Dithering: In the case of frequency dithering, DABSRC will be operated with multiple switching frequencies. Each switching frequency lasts for a certain period of time, named persisting time or dithering duty. Thereafter, it shifts to the next switching frequency and so on and finally returns to the initial switching frequency. This causes a periodic triangular variation in switching frequency with the time period termed as dithering time (T_o). Considering m different switching frequencies ($\omega_1, \omega_2, \ldots, \omega_k, \ldots, \omega_m$), $i_{\text{in}}(t)$ of each switching frequency operation is named from i_1 to i_m. The dithering duties of i_1–i_m are taken as d_1–d_m, respectively. Thus, from (3), i_k for kth switching frequency is expressed as

$$i_k = \frac{2I_{\text{pk}}}{\pi} - \frac{4I_{\text{pk}}}{\pi} \sum_{n=2,4,6}^{\infty} \frac{1}{n^2-1} \cos(n\omega_s t). \tag{4}$$

Now, a set of pulse functions y_1–y_m is considered to have duty cycles d_1–d_m, respectively, and has a frequency equal to the dithering frequency (f_o). Thus, $i_1 y_1$ denotes i_1 persisting for $d_1 T_o$ time. Similar is the case for i_2 in $i_2 y_2$ and i_k in $i_k y_k$. Therefore, the input current for the frequency dithering with m

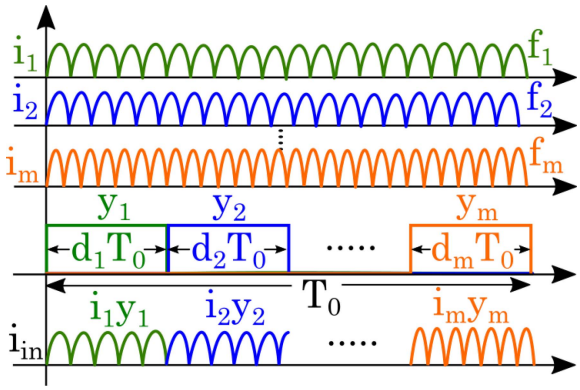

Fig. 2. Representation of the input current individually at different frequencies and with frequency dithering.

switching frequencies can be expressed as

$$i_{\text{in}}(t) = \sum_{k=1,2,3}^{m} i_k y_k. \tag{5}$$

Now, y_k can be expressed as

$$y_k(t) = \begin{cases} 1, \ \sum_{t=0}^{k-1} d_k T_o < t < \sum_{t=0}^{k} d_k T_o \\ 0, \ t < \sum_{t=0}^{k-1} d_k T_o \ \& \ \sum_{t=0}^{k} d_k T_o < t < T_o. \end{cases} \tag{6}$$

The Fourier series expansion of y_k is

$$y_k = d_k + \sum_{q=1}^{\infty} \frac{2}{q\pi} \sin(q\pi d_k) \cos(q\omega_o t - q\pi d_k). \tag{7}$$

Thus, $i_k y_k$, denoting the input current with FDT for kth switching frequency, is expressed in (8) shown at the bottom of this page. Term-I denotes a dc component, while Term-III denotes the dithering frequency and its harmonic components. Since the dithering frequency (ω_o) will be much lower in the range of 10 Hz, it will not be in the conducted EMI zone. Thus, Terms-I and III in (8) need not be considered in EMI analysis. The input current for individual frequencies and the same current after FDT are represented in Fig. 2. It can be inferred from (8) that in the conducted EMI zone along with the existing switching frequency harmonics at $n\omega_k$ represented by Term-II, additional frequency components are generated at $n\omega_k \pm q\omega_o$ called sidebands represented by Term-IV. Similarly, for every switching frequency ($\omega_1 - \omega_m$), the switching frequency harmonics and the sidebands will be generated.

The magnitude of the switching frequency harmonic components in single frequency operation is denoted by (A_n). The magnitude of the switching frequency harmonics using FDT is symbolized by $B_n^k (= d_k A_n)$, while that of sidebands is represented by C_{qn}^k. Here, q is the harmonic order of the dithering frequency. The magnitudes A_n from (3) and B_n^k and C_{qn}^k from (8) are expressed as

$$\begin{aligned} A_n &= \frac{4I_{\text{pk}}}{(n^2-1)\pi} \\ B_n^k &= d_k \frac{4I_{\text{pk}}}{(n^2-1)\pi} \\ C_{qn}^k &= \frac{4I_{\text{pk}}}{\pi^2} \frac{\sin(q\pi d_k)}{q(n^2-1)}. \end{aligned} \tag{9}$$

Although frequency dithering increases the number of switching frequencies, the sidebands are additionally generated. However, the magnitude B_n^k is lesser than A_n by a factor of d_k. Also, C_{qn}^k is comparatively smaller in value than B_n^k and A_n. Thus, the resultant magnitude (M_n) considering 9 kHz RBW will be lower than A_n. It can be inferred from (9) that the magnitudes of the various components can be regulated through d_k. The placement of the frequency components and their magnitude can be adjusted through dithering frequency and dithering duty selection.

B. Factors Affecting FDT

The FDT is affected by the mandated RBW of 9 kHz as well as the controller bandwidth.

1) Effect of RBW: RBW combines all the frequency components falling within the 9 kHz RBW window and generates the resultant magnitude of the combination.

As shown in Fig. 3, multiple frequency components are generated due to FDT and those falling within the span of 9 kHz are combined. Thus, the resultant magnitude can be expressed as

$$M_n = \sqrt{\sum (B_n^k)^2 + \sum (C_{qn}^k)^2}. \tag{10}$$

The resultant noise magnitude is M_n, which is higher than B_n^k or C_{mn}^k but will be lesser than A_n[13]. Thus, as RBW reduces the maximum achievable attenuation, it plays a significant role in designing the FDT.

2) Effect of Controller Bandwidth: FDT is also affected by the controller bandwidth. A higher dithering frequency and

$$\begin{aligned} i_k y_k = \underbrace{d_k \frac{2I_{\text{pk}}}{\pi}}_{\text{Term-I}} - \underbrace{d_k \frac{4I_{\text{pk}}}{\pi} \sum_{n=2,4,6,}^{\infty} \frac{1}{n^2-1} \cos(n\omega_s t)}_{\text{Term-II}} + \underbrace{\frac{2I_{\text{pk}}}{\pi} \sum_{q=1}^{\infty} \frac{2}{q\pi} \sin(q\pi d_k) \cos(q\omega_o t - q\pi d_k)}_{\text{Term-III}} \\ \underbrace{- \frac{4I_{\text{pk}}}{\pi^2} \times \left\{ \sum_{n=2,4,6,}^{\infty} \sum_{q=1}^{\infty} \frac{1}{q(n^2-1)} \sin(q\pi d_k) \left\{ \cos\{(n\omega_k + q\omega_o)t - q\pi d_k\} + \cos\{(n\omega_k - q\omega_o)t + q\pi d_k\} \right\} \right\}}_{\text{Term-IV}}. \end{aligned} \tag{8}$$

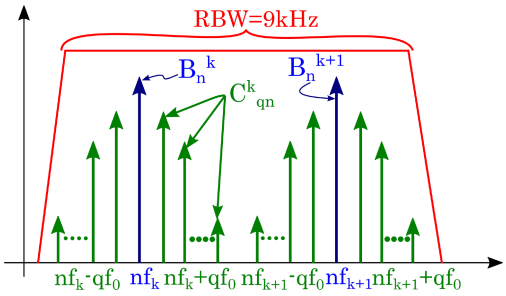

Fig. 3. Resultant of frequency components within 9 kHz RBW.

lower dithering duty will cause a fast change in the switching frequency. In case, the persisting time of each frequency is lower than the settling time of load or input transients. The effective settling time will increase as the controller considers the frequency change as a separate transient condition. This is due to the dependence of output variables on frequency. Thus, the frequency dithering will cause a large ripple in the output variables. As the controller will be ineffective in reaching the steady state.

Thus, to achieve maximum attenuation of EMI noise magnitude, the switching frequency, dithering frequency, and dithering duty need to be selected with the following objectives.

1) Minimizing the frequency components within RBW.
2) Eliminating the effect of control bandwidth on FDT.

C. Proposed FDT

The parameters of the proposed FDT are selected based on the abovementioned factors governing the EMI attenuation.

1) Switching Frequency Selection: The designed DABSRC has a resonant frequency of 61 kHz. Thus, as per [21] and [27], the optimum operational switching frequency range can be 1.08–1.2 times the resonant frequency, which comes to be 66–73 kHz to reduce losses [21]. As per (8), $i_k y_k$ and subsequently i_{in} have even harmonics of switching frequency components. This will make the fourth harmonics of the switching frequency fall in the conducted EMI zone, as it goes above 150 kHz. In order to maximize the EMI attenuation, the aim is to select the switching frequencies in a way such that fourth harmonic component of only one of the selected switching frequencies falls in a 9 kHz RBW window. Thus, to keep fourth harmonic component of two subsequent switching frequencies 9 kHz apart, the frequency gap (Δf_4) between fourth harmonic component of two subsequent switching frequencies should be $\Delta f_4 > 9$ kHz. This will make the frequency gap between two subsequent switching frequencies to be $\Delta f > 2.25$ kHz. Thus, considering Δf of 2.5 or 3 kHz, only three switching frequencies can be selected in the operational frequency range of 66–73 kHz, which spans only over 8 kHz. The maximum attenuation possible with three switching frequencies can be of 9.5 dB based on the formula, $A_{r(\max)} = 20\log(1/m)$ [13]. Here, $A_{r(\max)}$ and m denote maximum attenuation and number of switching frequencies, respectively. However, the sidebands falling within the 9 kHz RBW considerably affect the attenuation achieved by the FDT. Due to the higher number of sidebands falling within the 9 kHz RBW, the actual attenuation (A_r) will be significantly lower than $A_{r(\max)}$ [13]. In addition, 2.5 or 3 kHz, being a higher step change in frequency, will increase the overshoot/undershoot and settling time of output voltage and reactive power due to higher frequency step-change. Both of these factors bring the need to increase the number of switching frequencies and reduce the frequency step-change as well.

Thus, to increase the number of switching frequency components and attenuation, the alternative is to keep fourth harmonic component of two subsequent switching frequencies within the RBW window. This makes the frequency gap between the fourth harmonic components of two subsequent switching frequencies to be $\Delta f_4 > 4.5$ kHz. Thus, the step-change between two subsequent switching frequencies becomes $\Delta f > 1.125$ kHz. Thus, considering the switching frequency to be f_{1-5} and with $\Delta f = 1.5$ kHz, five switching frequencies can be selected as

$$f_1 = 66,\ f_2 = 67.5,\ f_3 = 69,\ f_4 = 70.5,\ f_5 = 72 \text{ kHz}.$$

Thus, with five switching frequencies, $A_{r(\max)} = 20\log(1/m) = 14$ dB. However, because of the sidebands arising out of frequency dithering, the achieved A_r will be lesser than $A_{r(\max)}$. The effective EMI attenuation A_r can be calculated considering the sidebands, which need the selection of dithering frequency and dithering duty.

2) Dithering Frequency and Duty Selection: The dithering frequency dictates the rate of change of switching frequency. A higher dithering frequency leads to faster variation in the switching frequency, which affects the controller bandwidth. In case the switching frequency varies within the settling time of the converter during any load or input transient, the control will be unable to reach the steady state. Thus, since the proposed control algorithm achieves a settling time of 5 ms, the persisting time of each frequency is kept higher than 5 ms. At the same time, to eliminate large transients in converter state variables due to higher step-change in frequency, continuous triangular switching frequency variation is chosen. Thus, to accommodate the load transient setting time within the persisting time of each frequency, the persisting time is selected as 10 ms. Hence, for triangular frequency variation, the dithering time and frequency come to be $T_0 = 4 \times 10 + 10 = 90$ ms and $f_0 = 11$ Hz, respectively. Thus, the dithering duty of the five switching frequency to be $d_1 = d_2 = d_3 = d_4 = 2\left(\frac{10}{90}\right) = 0.22$, and $d_5 = \left(\frac{10}{90}\right) = 0.11$.

3) EMI Attenuation: The EMI attenuation is calculated for the fourth harmonics component of f_1–f_5 as these are the first frequency components in the conducted EMI zone. Also, the filter is to be designed based on the initial frequency region [13]. Now, within the 9 kHz RBW, the frequency components $4f_1$, $4f_2$, and their respective sidebands fall. Therefore, the resultant magnitude considering till the significant 21st harmonic of

sidebands is calculated using (8)–(10) as

$$M_4 = \sqrt{\begin{aligned}&(B_4^1)^2 + 2\sum_{q=1}^{21}(C_{q4}^1)^2 \\ &+ (B_4^2)^2 + 2\sum_{q=1}^{21}(C_{q4}^2)^2.\end{aligned}} \tag{11}$$

Thus, the attenuation (A_r) at the fourth harmonic region of switching frequencies can be calculated as $A_r = \frac{A_4}{M_4} \simeq 7$ dB. Here, B_4^1 and B_4^2 denote the magnitude of fourth harmonic components of f_1 and f_2, while C_{q4}^1 and C_{q4}^2 denote corresponding sidebands, respectively.

The FDT in DABSRC causes variation in the state variables because of its dependence on switching frequency. This varies the output variables, which demands a frequency-independent control system to regulate the output voltage and reactive power simultaneously. The next section describes the modified large-signal model-based control technique to assist frequency dithering in DABSRC.

IV. Control Algorithm

The large-signal modeling of DABSRC is presented, and then represented into active and reactive power control models separately. Thereafter, the estimation of active and reactive components of the HF-link current is performed. Finally, the control algorithm is formulated, including the feedforward terms, which makes the control transfer functions independent of switching frequency.

A. Large Signal Modeling

The DABSRC circuit diagram shown in Fig. 1 has been simplified using the fundamental harmonic approximation (FHA) [21], [27]. The FHA equivalent circuit and timing diagrams are shown in Fig. 4(a). Here, v_a and v_b denote input and output bridge voltages, respectively, and v_c is capacitor voltage. In Fig. 1, S_1–S_4 denote the switching devices of primary-side bridge and P_1–P_4 denote the switching devices of secondary-side bridge. The external phase-shift between the input and output bridges is denoted by ϕ, which is phase-shift or time-lag between the turn-ON instants of S_1 and P_1. Here, S_1–S_4 are operated at ω_s switching frequency at 50% duty-ratio. S_2 and S_3 are switched complementary to S_1 and S_4, respectively. In this case of square-wave operation of the input-bridge, S_1 and S_4 are turned ON simultaneously. The variable, θ, denotes the internal phase-shift of the output bridge, which is essentially the phase-shift or the time-lag between the turn-ON instants of P_1 and P_4. Here, P_1–P_4 are operated at ω_s switching frequency at 50% duty-ratio. P_2 and P_3 are switched complementary to P_1 and P_4, respectively. The variables ϕ and θ are shown in the timing diagram of DABSRC in Fig. 4(b). The resonant tank comprises a series connected inductance (L_s), capacitance (C_s), and equivalent resistance (R_s) and HF transformer. As per FHA, considering the fundamental components, the large-signal state

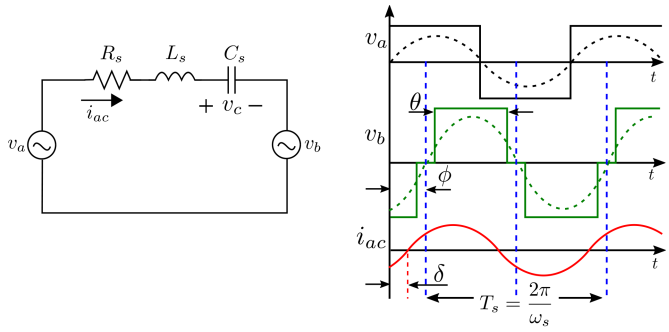

(a) (b)

Fig. 4. (a) Equivalent circuit diagram. (b) Timing diagram of DABSRC.

equations are

$$\begin{aligned} L_s\frac{di_{\text{ac}}}{dt} &= v_a - v_b - R_s i_{\text{ac}} - v_c \\ C_s\frac{dv_c}{dt} &= i_{\text{ac}}. \end{aligned} \tag{12}$$

The output current equation from Fig. 1 can be written as

$$C_f\frac{dv_o}{dt} = i - \frac{v_o}{R_o}. \tag{13}$$

Now, the variables can be represented as a summation of $\sin\omega_s t$ and $\cos\omega_s t$ terms as follows:

$$\begin{aligned} v_a &= kV_{\text{in}}\sin\omega_s t = v_{aa}\sin\omega_s t \\ v_b &= kV_o\sin(\omega_s t - \phi) = v_{ba}\sin\omega_s t + v_{br}\cos\omega_s t \\ i_{\text{ac}} &= I_{\text{ac}}\sin(\omega_s t - \delta) = i_a\sin\omega_s t + i_r\cos\omega_s t \\ v_c &= V_c\sin(\omega_s t - \beta) = v_{ca}\sin\omega_s t + v_{cr}\cos\omega_s t. \end{aligned} \tag{14}$$

The coefficients of $\sin\omega_s t$ and $\cos\omega_s t$ are the active and reactive variables represented by subscripts "a" and "r," respectively. The active–reactive variables are expressed as

$$\begin{aligned} v_{aa} &= kV_{\text{in}} \\ v_{ba} &= kV_o\cos\theta\cos\phi, \quad & v_{br} &= -kV_o\cos\theta\sin\phi \\ i_a &= I_{\text{ac}}\cos\delta, & i_r &= -I_{\text{ac}}\sin\delta \\ v_{ca} &= V_c\cos\beta, & v_{cr} &= -V_c\sin\beta. \end{aligned} \tag{15}$$

The rectified output current (i) can be expressed by using the power balance at the output bridge as

$$i = \int_{\phi T_s}^{\phi(1+T_s)} i_{\text{ac}}dt = \frac{2}{\pi}(i_a\cos\phi - i_r\sin\phi). \tag{16}$$

The state equations in terms of active–reactive variables from (12) can be written as

$$\begin{aligned} L_s\frac{di_a}{dt} &= \omega_s L_s i_r - R_s i_a - v_{ca} + v_{aa} - v_{ba} \\ L_s\frac{di_r}{dt} &= -\omega_s L_s i_a - R_s i_a - v_{cr} - v_{br} \\ C_s\frac{dv_{ca}}{dt} &= \omega_s C_s v_{cr} + i_a \\ C_s\frac{dv_{cr}}{dt} &= -\omega_s C_s v_{ca} + i_r. \end{aligned} \tag{17}$$

Similarly, the output state equation from (13) can be written as

$$C_f\frac{dv_o}{dt} = \frac{2}{\pi}(i_a\cos\phi - i_r\sin\phi) - \frac{v_o}{R_o}. \tag{18}$$

Now, two equivalent state-space representations can be obtained from (17) representing active and reactive power separately. Through the phasor expansion of the converter variables, the active power (P) can be related to $I_a = I_{\text{ac}}\cos\delta$ as

$$\begin{aligned} P &= \text{Re}[\vec{V}_a\vec{I}^*_{\text{ac}}] = \text{Re}[(V_a\angle 0)(I_{\text{ac}}\angle -\delta)^*] \\ &= \text{Re}\left[\frac{\pi}{2}V_{\text{in}}I_{\text{ac}}(\cos\delta + j\sin\delta)\right] \\ &= \frac{\pi}{2}V_{\text{in}}I_{\text{ac}}\cos\delta \\ &= \frac{\pi}{2}V_{\text{in}}I_a \\ \Rightarrow I_a &= \frac{2}{\pi}\frac{P}{V_{\text{in}}}. \end{aligned} \tag{19}$$

Similarly, reactive power (Q) can be related to $I_r = -I_{\text{ac}}\sin\delta$ as

$$\begin{aligned} Q &= \text{Im}[\vec{V}_a\vec{I}^*_{\text{ac}}] = \text{Im}[(V_a\angle 0)(I_{\text{ac}}\angle -\delta)^*] \\ &= \text{Im}\left[\frac{\pi}{2}V_{\text{in}}I_{\text{ac}}(\cos\delta + j\sin\delta)\right] \\ &= \frac{\pi}{2}V_{\text{in}}I_{\text{ac}}\sin\delta \\ &= -\frac{\pi}{2}V_{\text{in}}I_r \\ \Rightarrow I_r &= -\frac{2}{\pi}\frac{Q}{V_{\text{in}}}. \end{aligned} \tag{20}$$

Thus, the active and reactive power control can be achieved by controlling i_a and i_r, respectively. This necessitates estimating the same from i_{ac}, manifested in the next section.

B. Estimation of Active–Reactive Variables

The active–reactive current components (i_a and i_r) are estimated from i_{ac} for the continuous switching frequency variation. The estimation uses the sensed current ($i_1 = i_{\text{ac}}$) and the unit vectors ($\sin\omega_s t$ and $\cos\omega_s t$), which are generated from the microcontroller through DAC as per the switching frequency variation. A new variable i_2 is generated from i_1 by integrating

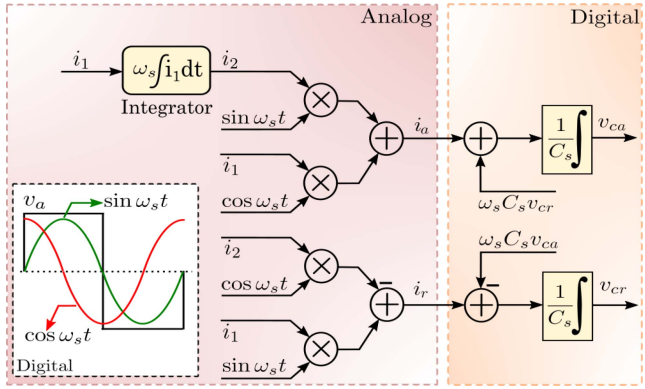

Fig. 5. Estimation of i_a, i_r, v_{ca}, and v_{cr} independent of switching frequency.

i_1 and multiplying by ω_s. Thus, i_1 and i_2 can be expressed as

$$\begin{aligned} i_{\text{ac}} = i_1 &= I_{\text{ac}}\sin(\omega_s t - \delta) \\ i_2 &= \omega_s\left(\int I_{\text{ac}}\sin(\omega_s t - \delta)dt\right) \\ &= -I_{\text{ac}}\cos(\omega_s t - \delta). \end{aligned} \tag{21}$$

Now, i_a and i_r can be expressed as

$$\begin{aligned} i_a &= i_1\cos\omega_s t + i_2\sin\omega_s t \\ i_r &= i_1\sin\omega_s t - i_2\cos\omega_s t. \end{aligned} \tag{22}$$

Now, putting (22) in (17), v_{ca} and v_{cr} can be estimated as

$$\begin{aligned} v_{ca} &= \frac{1}{C_s}\int(i_a + \omega_s C_s v_{cr})dt \\ v_{cr} &= \frac{1}{C_s}\int(i_r - \omega_s C_s v_{ca})dt. \end{aligned} \tag{23}$$

The estimation of i_a and i_r are carried out in the analog domain to reduce the complexity and eliminate the requirement of high-speed ADCs for sensing i_{ac}. While v_{ca} and v_{cr} are estimated in the digital domain in digital signal processor (DSP). This requires sensing i_a and i_r, which can be performed using the internal ADC of DSP, as they are primarily dc components. The integrators are aided with a low-pass filter having a cutoff frequency of ten times the switching frequency. The estimation is represented in Fig. 5. The DSP internal ADCs have a sampling time of 50 μs, which can be modeled as a first-order LPF with a single pole (ω_1) at 20 kHz. The switching frequency is kept at 66 kHz, and the controller bandwidth is selected 10 times less, around 6.6 kHz. Thus, in the case of low-frequency variation, the ADC sampling time does not interfere with the controller bandwidth.

In Fig. 6(a) and 6(b), the percentage error is shown between the actual and estimated i_a and i_r at various switching frequencies. The error is calculated by samples of i_a and i_r at three different loading conditions over the switching frequency variation range. The maximum error is below 6% even at 25% loading, which is in the acceptable range [21], [27].

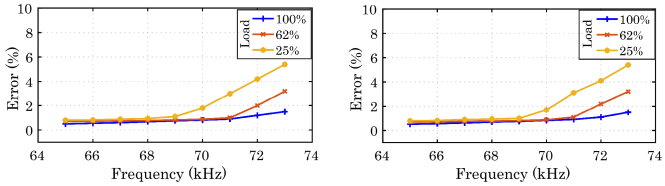

Fig. 6. Error of (a) i_a and (b) i_r with switching frequency variation.

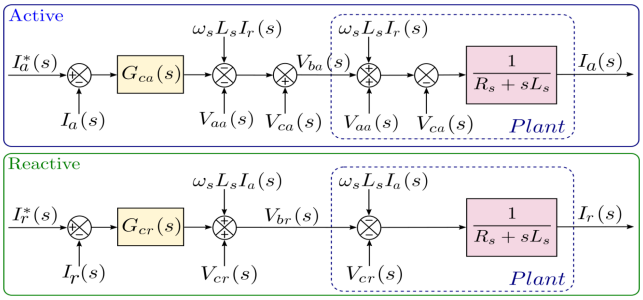

Fig. 7. Control block diagram for active and reactive current control loops.

C. Control System Design

The modified large-signal model-based control (MLSMC) comprises two inner control loops for controlling active and reactive currents, i_a and i_r. In addition, an outer voltage control loop is presented to regulate output voltage. The reactive current reference is fixed at zero, which makes the output voltage dependent on i_a alone. So, the output of the voltage control loop provides the reference of the active current control loop ($I_a^*(s)$). The reactive current being zero minimizes the reactive power flow in the HF ac link, which satisfies the condition of minimum rms current and zero voltage switching (ZVS) operation. The inner active–reactive current control loops produce the active–reactive component of v_b, v_{ba}, and v_{br}, respectively. In this control method, the double-phase-shift modulation technique is adopted, where ϕ and θ are modulated.

1) Current Controller: The plant model for the current control design is obtained by Laplace transform of (17), and the plant transfer functions can be written as

$$\left.\begin{aligned} G_{va}(s) &= \frac{I_a(s)}{V_{ba}(s)}\Big|_{\substack{V_{ca}(s)=0\\V_{aa}(s)=0\\I_r(s)=0}} \\ G_{vr}(s) &= \frac{I_r(s)}{V_{br}(s)}\Big|_{\substack{V_{cr}(s)=0\\I_a(s)=0}} \end{aligned}\right\} = \frac{1}{R_s+sL_s}. \tag{24}$$

The plant transfer function for active and reactive current control loops are denoted by $G_{va}(s)$ and $G_{vr}(s)$, respectively. The terms $V_{ca}(s)$, $V_{cr}(s)$, $V_{aa}(s)$, $\omega_s L_s I_a(s)$, and $\omega_s L_s I_r(s)$ constitute the feedforward terms and do the cancellation. Due to the feedforward cancellation technique, $G_{va}(s)$ and $G_{vr}(s)$ become independent of switching frequency and operating points. The active–reactive current control loops have been shown in Fig. 7.

Since $G_{va}(s)$ and $G_{vr}(s)$ are first-order, the regular proportional–integral controllers ($G_{ca}(s)$ and $G_{cr}(s)$) can achieve the control, which is of the form

$$G_{ca}(s) = G_{cr}(s) = K_{pi} + \frac{K_{ii}}{s}. \tag{25}$$

The parameters K_{pi} and K_{ii} can be designed using the chosen crossover frequency (ω_{ci}). The Bode plots of $G_{va}(s)$, $T_{ca}(s) = G_{va}(s)G_{ca}(s)$, and $\frac{G_{va}(s)}{1+G_{va}(s)G_{ca}(s)}$ are shown in Fig. 8(a). Since the switching frequency (f_s) varies from 66 to 72 kHz, ω_{ci} is fixed at 38.9 krad/s ($= 2\pi 6.6$ kHz), which is 1 decade lower than the lowest switching frequency of 66 kHz. The gain, $|G_{va}(j\omega_{ci}|$, is compensated by designing the controller gain to $|G_{ca}(j\omega_{ci})| = -|G_{cr}(j\omega_{ci})| = -10.6$ dB. Now, using the pole-zero cancellation method, the PI-controller parameters are $K_{\text{pi}} = 3.2$ and $K_{ii} = 30230$. This places ω_{ci} of $T_{ca}(s)$ at the desired frequency. The plot of closed-loop transfer function $\frac{G_{va}(s)}{1+G_{va}(s)G_{ca}(s)}$ remains below 0 dB as well, making it efficient in disturbance rejection. As $G_{va}(s)$ and $G_{vr}(s)$ are independent of switching frequency, $G_{ca}(s)$ and $G_{cr}(s)$ can control i_a and i_r, irrespective of switching frequency variation. $G_{cr}(s)$ can be designed similar to $G_{ca}(s)$.

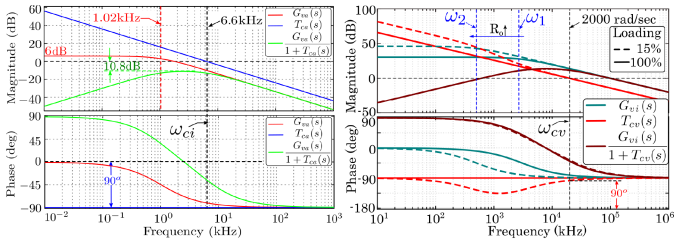

Fig. 8. Bode plot of (a) i_a current control loop and (b) voltage control loop.

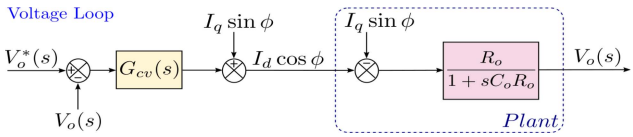

Fig. 9. Control block diagram for voltage loop.

2) Voltage Controller: The plant model is obtained by the Laplace transform of (18), which is

$$G_{vi}(s) = \frac{V_o(s)}{I_a'(s)}\Big|_{I_r'(s)=0} = \frac{\pi}{2}\left(\frac{R_o}{1+sC_fR_o}\right) \tag{26}$$

where $I_a'(s) = I_a(s)\cos\phi$ and $I_r'(s) = I_r(s)\sin\phi$. C_o denotes output capacitance, R_o denotes load resistance, and $I_r'(s)$ is the feedforward term. The voltage control loop has been depicted in Fig. 9. The Bode plots of plant ($G_{vi}(s)$), controller ($G_{cv}(s)$), and disturbance rejection $\left(\frac{G_{vi}(s)}{1+G_{cv}(s)G_{vi}(s)}\right)$ transfer functions are shown in Fig. 8(b). $G_{vi}(s)$ being first order system, a PI controller ($G_{cv}(s)$) is chosen for the control. The setting time (T_s) is kept at 5 ms [2], [28], which also equals 10τ where τ is the time-constant of loop gain ($T_{cv}(s) = G_{cv}(s)G_{vi}(s)$).

In case of the first-order transfer function, the settling time $T_s = 10\tau = 5$ ms, which makes $\tau = 0.2$ ms, where τ is the time

constant of the system. Thus, GCF (ω_{cv}) comes out to be $\omega_{cv} = \tau^{-1} = 2000$ rad/s. Here, ω_{cv} is considered to be the bandwidth of the system. The controller gain required at ω_{cv} is $|G_{cv}(j\omega_{cv})| = -|G_{vi}(j\omega_{cv}| = -16.5$ dB, which is obtained by $K_{pv} = 0.25$ and $K_{iv} = 52$. As shown in Fig. 8(b), with increasing R_o, the pole $\left(\frac{1}{R_o C_f}\right)$ shifts to the left side, which does not affect ω_{cv}, as it is always higher $\frac{1}{R_o C_f}$. Thus, as evident from Fig. 8(b), for 15% and 100% loading, ω_{cv} and phase-margin does not vary.

The phase-shifts, ϕ and θ, are generated from v_{ba}, v_{br}, and v_o as

$$\phi = \tan^{-1}\left(\frac{v_{br}}{v_{ba}}\right)$$
$$\theta = \cos^{-1}\left(\frac{\pi}{4}\frac{\sqrt{v_{br}^2 + v_{ba}^2}}{v_o}\right). \quad (27)$$

V. Experimental Results

This section experimentally validates the proposed frequency dithering along with the control technique on a 1.5 kW SiC-based DABSRC hardware prototype.

A. Hardware Prototype

The selected SiC MOSFETs are C3M0065100 K, which has a rated blocking voltage of 1 kV and drain current of 35 A. The proposed FDT and the control algorithm are implemented using a TMS320F28335 DSP and a Cyclone IV field-programmable-gate-array-based hybrid platform. The generation of i_a and i_r from i_{ac} are carried out in the analogue domain. The DABSRC is designed with the available series inductance and capacitance of 62 μH and 0.11 μF, respectively, making the resonant frequency 61 kHz. The switching frequency variation is within 66–73 kHz, considering the validity of FHA [21]. In single-switching frequency operation, DABSRC is operated at 66 kHz. The input and output dc-bus capacitances are 100 μF. The hardware setup, along with the EMI measuring setup, is shown in Fig. 10(a) and (b), respectively.

B. Frequency Dithering Technique

The proposed FDT, with and without the variable frequency control, is implemented in a DABSRC prototype and experimentally validated at 1.5 kW power rating. The CM and DM noise are shown in Fig. 11(a) and (b), respectively. It can be observed that there is an attenuation of 7 and 8 dB in DM and CM noise, respectively, as compared to single-switching frequency operation. The same has been mathematically calculated in Section III-C3. As shown in Fig. 11(a), after implementing the proposed FDT, the DM noise level goes below the specified EMI noise limit in CISPR-11 throughout the conducted EMI frequency range of 0.15–30 MHz. This eliminates the requirement of a DM filter to attenuate EMI noise at a power rating of as high as 1.5 kW. Since the CM noise does not pass the CISPR-11 standard, as shown in Fig. 11(b), an additional CM filter will be required for complete CM noise attenuation. However, the achieved 8 dB attenuation

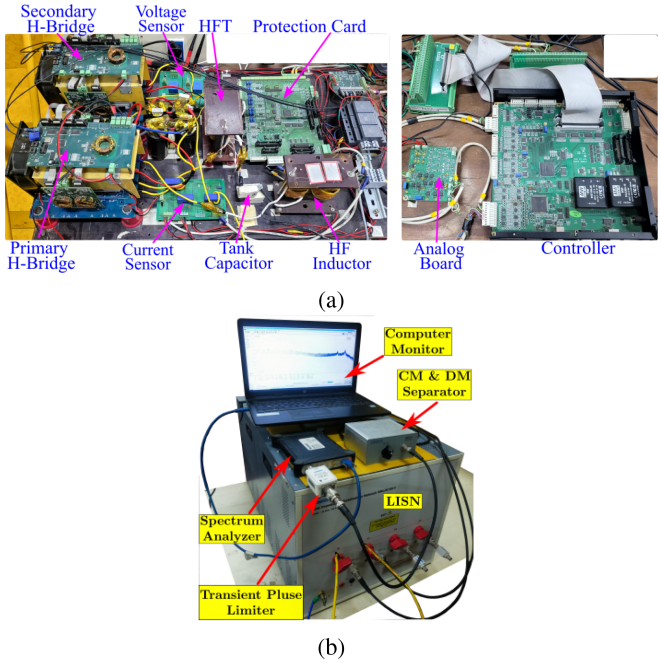

Fig. 10. (a) DABSRC hardware setup. (b) EMI measuring equipment.

in CM noise will cause a significant reduction in filter size by 34% compared to single-frequency operation. The CM filter size reduction has been validated through a conventional filter design in Section V-D. The input current in Fig. 11(c) is routed through LISN.

C. Control Algorithm

The MSLMC technique has been validated experimentally in this section. Fig. 12(a) shows the response of the DABSRC state and output variables to continuous frequency variation or frequency dithering in open-loop conditions. It can be observed that with the variation in f_{sw}, the output variables v_o, i_a, and i_r also vary in a similar fashion as expected. The output voltage varies from 270 to 310 V for a frequency variation from 66 to 72 kHz with a constant load. The required nominal voltage is 300 V, with the allowed fluctuation for most of the applications being $\pm 5\%$ [2], [28]. However, in Fig. 12(a), the voltage fluctuation is $\pm 13.5\%$, which is unsuitable for the applications. Also, the variation of reactive power increases losses. Therefore, with the proposed control technique as shown in Fig. 12(b), for the same variation of f_{sw}, the output variables v_o, i_a, and i_r are constant for a fixed load. The output voltage is fixed to the nominal value of 300 V ($\pm 2\%$), and i_r is regulated at zero irrespective of frequency dithering. The transient response of the converter is shown in Fig. 12(c), which shows a settling time of 5 ms for v_o, i_a, and i_r subjected to 62.5% step-load change. In Fig. 12(d)–(f), the reactive power at three different switching frequencies varies due to frequency dithering in open-loop even with constant load. Since reactive power depends on switching frequency as well, however, with the closed-loop control, it becomes constant with switching frequency variation at any given load, as shown in Fig. 12(g)–(i).

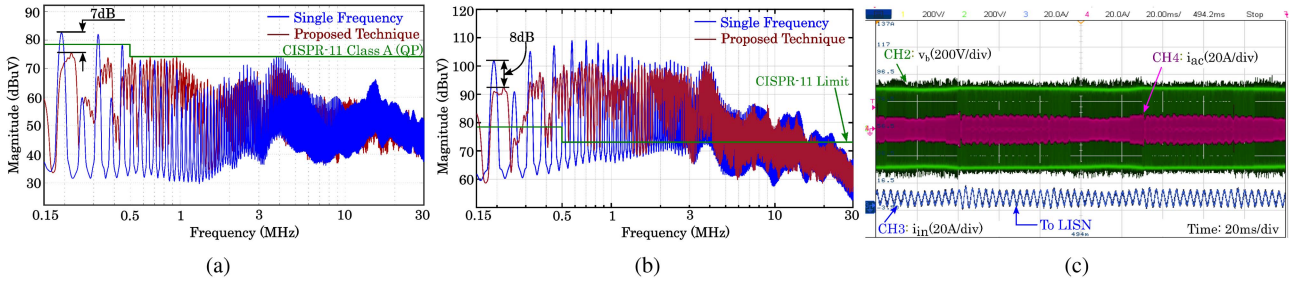

Fig. 11. Experimental results in steady-steate. (a) DM noise spectrum. (b) CM noise spectrum. (c) v_a, v_b, i_{ac}, and i_{in}(measured by LISN and spectrum analyzer).

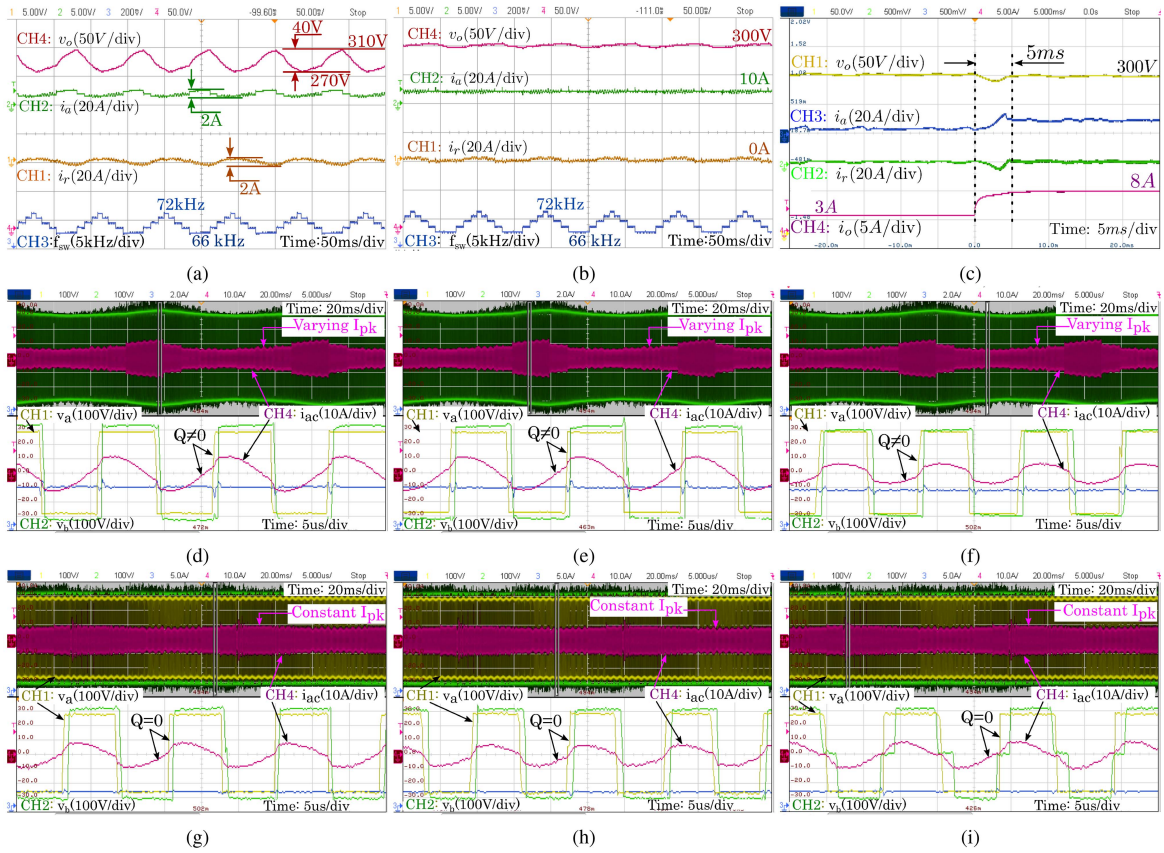

Fig. 12. Experimental results showing v_o, i_a, i_r, and f_{sw} with frequency dithering. (a) Open-loop. (b) Closed-loop. (c) Transient response showing v_o, i_a, i_r, and i_o for 62.5% step-load change. Waveforms of v_a, v_b, and i_{ac} showing reactive power condition at three different switching frequency in case of frequency dithering. (d)–(f) Open-loop. (g)–(i) Closed-loop.

D. Filter Size Reduction

As the DM filter is eliminated, the design of the CM filter has been shown. As per [29], the required attenuation for the CM noise (A_r) in dB μV can be calculated as

$$A_r[\text{dB}\mu\text{V}] = A_{\text{CM}}[\text{dB}\mu\text{V}] + 6\ \text{dB}\mu\text{V} - A_{\text{lim}}[\text{dB}\mu\text{V}] \quad (28)$$

where $A_{\text{CM}}[\text{dB}\mu\text{V}]$ is the actual noise value, 6 dBμV is the considered safety factor, and $A_{\text{lim}}[\text{dB}\mu\text{V}]$ is the international noise limit as per CISPR-11 Class A (QP) [7]. A regular second-order *LC* filter, as shown in Fig. 13, has been chosen.

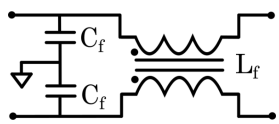

Fig. 13. Conventional CM filter circuit diagram.

The filter parameters are designed for both single-frequency operation and with the proposed FDT.

1) Single Frequency Operation: A_r from (28) comes out to be $A_r = 102 + 6 - 79 = 29$ dBμV, required at the first peak position of 190 kHz. Thus, the second-order filter having

TABLE I
PERFORMANCE COMPARISON OF THE PROPOSED METHOD AGAINST EXISTING TECHNIQUES

FDT	Converter Topology	Performance Parameters				
		Frequency Range (KHz)	Sidebands Considered	RBW Value (As per CISPR-11)	Attenuation (dB)	Control Variables
Spread Spectrum with Single Phase-Shift [16]	Current-Fed *LLC*	24	No	- (No)	22	Output Voltage
Spread Spectrum with Single Phase-Shift [17]	Half-Bridge *LLC*	80	No	- (No)	25	Output Voltage
Spread Spectrum with Hybrid Modulation [14]	*LLC*	14	No	100 Hz (No)	16	Output Voltage
Spread Spectrum with Single Phase-Shift [15]	*LLC*	13.5	No	100 Hz (No)	12	Output Voltage
Spread Spectrum with Single Phase-Shift [18]	DAB	10	No	- (No)	12	Output Voltage
Spread Spectrum with Ripple Rejection Control [19]	*LLC*	10	No	100 Hz (No)	17	Output Voltage
Spread Spectrum with Pulsewidth Modulation [20]	Current-Fed *CLLC*	70	No	9 kHz (Yes)	4	Output Voltage
Proposed Method	DABSRC	6	Yes	9 kHz (Yes)	8	Output Voltage, Reactive Power

40 dB/decade slope should have a cutoff frequency at 35 kHz. Thus, considering $C_f = 2.2$ nF, L_f becomes 9 mH.

2) Proposed FDT: After implementing the proposed FDT, A_r can be calculated form (28) as $A_r = 93 + 6 - 79 = 21$ dBμV. Also, the first noise peak shifts to 220 kHz, which makes the cutoff frequency becomes 65 kHz. Thus, with $C_f = 2.2$ nF, the required L_f is 2.5 mH.

It can be observed that the filter inductor value is reduced by as high as 77% on implementing the proposed FDT as compared to single-frequency operation. This causes an inductor size reduction by 34% based on the market-available inductors [30], [31]. Since the inductor size dominates in any filter topology, the reduction in filter size can be directly related [13].

VI. PERFORMANCE COMPARISON

The proposed technique is compared against the existing techniques, as shown in Table I. The technique in [14] achieves 16 dB attenuation and output voltage regulation in an *LLC* resonant converter with a wide switching frequency variation of 14 kHz. It deviates the switching frequency far from the resonant frequency, producing a higher voltage ripple. Similarly, in [16], 22 dB attenuation is reported in a current-fed *LLC* converter with a frequency variation of 24 kHz. In [17], 25 dB attenuation is achieved with frequency variation of 80 kHz in a half-bridge *LLC* converter through partial power processing concept. A similar FDT with improved phase-shift control for DAB in [18] achieves 12 dB attenuation with 10 kHz frequency variation. In [15], an *LLC* converter achieves 12 dB attenuation with a frequency variation of 13.5 kHz. Ripple rejection control technique in [19] for *LLC* converter achieves 17 dB reduction with 10 kHz variation. However, none of the methods considers the RBW of 9 kHz mandated by CISPR-11. In [20], only 4 dB attenuation is achieved considering 9 kHz bandwidth in a CLLC converter through pulse-width modulation. However, all the abovementioned methods achieve only output voltage control. The reactive power control is not attempted, which increases the losses. The wide switching frequency variation in the reported literature will increase the losses in DABSRC, whereas, the proposed technique achieves 8 dB attenuation considering 9 kHz RBW with a narrow frequency variation of 7 kHz. It also achieves control of both output voltage and reactive power independent of switching frequency.

VII. CONCLUSION

This article proposes an FDT combined with frequency-independent control to attenuate EMI and eliminate the effect of frequency dithering on state variables in a DABSRC. The switching frequency in the proposed technique is varied over a range of 7 kHz from 66 to 72 kHz in steps of 1.5 kHz. The switching frequencies and dithering frequency are selected considering the effect of 9 kHz RBW as mandated by CISPR-11. This article also proposes a modified large-signal model-based control technique to regulate the output voltage and reactive power irrespective of frequency dithering. This removes the dependence of state variables of DABSRC on switching frequency. The proposed technique achieves around 8 dB attenuation in DM and CM noise, which achieves a CM filter size reduction by 34% and eliminates the DM filter. The control technique achieves output voltage and reactive power regulation independent of frequency dithering along with load transient settling time of 5 ms for as high as 62.5% step-load change. The achieved results are validated experimentally on a 1.5 kW DABSRC prototype.

REFERENCES

[1] F. Krismer, J. Biela, and J. Kolar, "A comparative evaluation of isolated bi-directional DC/DC converters with wide input and output voltage range," in *Proc. 40th IAS Annu. Meeting. Conf. Rec. 2005 Ind. Appl. Conf.*, 2005, pp. 599–606.

[2] J. M. Crider and S. D. Sudhoff, "Reducing impact of pulsed power loads on microgrid power systems," *IEEE Trans. Smart Grid*, vol. 1, no. 3, pp. 270–277, Dec. 2010.

[3] G. Liu, Y. Jang, M. M. Jovanović, and J. Q. Zhang, "Implementation of a 3.3-kW DC–DC converter for EV on-board charger employing the series-resonant converter with reduced-frequency-range control," *IEEE Trans. Power Electron.*, vol. 32, no. 6, pp. 4168–4184, Jun. 2017.

[4] S. Bhawal, S. S. Chakraborty, and K. Hatua, "Dynamic modeling and closed-loop control of a solid-state transformer (SST) based on series resonant converter (SRC)," *IEEE Trans. Emerg. Sel. Topics Power Electron.*, vol. 10, no. 4, pp. 3733–3745, Aug. 2022.

[5] D. Han, S. Li, Y. Wu, W. Choi, and B. Sarlioglu, "Comparative analysis on conducted CM EMI emission of motor drives: WBG versus Si devices," *IEEE Trans. Ind. Electron.*, vol. 64, no. 10, pp. 8353–8363, Oct. 2017.

[6] T. Li, J. Gudex, R. Olson, H. Abdallah, R. M. Cuzner, and J. Katcha, "Modeling and validation of common-mode emissions of SiC MOSFET-based voltage source inverter motor drive," in *Proc. 2023 IEEE Appl. Power Electron. Conf. Expo.*, 2023, pp. 56–63.
[7] CISPR 11:2024, *Industrial, Scientific and Medical Equipment–Radio Frequency Disturbance Characteristics – Limits and Methods of Measurement*, Standard ICS 33.100.10, International Electrotechnical Commission, Geneva, Switzerland, 2021.
[8] G. Ala, G. C. Giaconia, G. Giglia, M. C. Di Piazza, and G. Vitale, "Design and performance evaluation of a high power-density EMI filter for PWM inverter-fed induction-motor drives," *IEEE Trans. Ind. Appl.*, vol. 52, no. 3, pp. 2397–2404, May/Jun. 2016.
[9] Z. Zhang and A. M. Bazzi, "A virtual impedance enhancement based transformer-less active EMI filter for conducted EMI suppression in power converters," *IEEE Trans. Power Electron.*, vol. 37, no. 10, pp. 11962–11973, Oct. 2022.
[10] C.-H. Moon, C.-J. Chen, and S.-W. Lee, "A random modulation spread-spectrum digital PWM for a low system clock digital buck converter," *IEEE Access*, vol. 9, pp. 156663–156671, 2021.
[11] J. Chen, D. Jiang, Z. Shen, W. Sun, and Z. Fang, "Uniform distribution pulsewidth modulation strategy for three-phase converters to reduce conducted EMI and switching loss," *IEEE Trans. Ind. Electron.*, vol. 67, no. 8, pp. 6215–6226, Aug. 2020.
[12] S. Nayak, V. Pandey, and K. Hatua, "A dithering technique for mitigation of conducted emission noise of SiC MOSFET based VSI driving an induction motor," *IEEE Trans. Power Electron.*, vol. 39, no. 2, pp. 2281–2293, Feb. 2024.
[13] S. Nayak, V. Pandey, and K. Hatua, "A dithering technique for mitigation of differential mode noise of SiC MOSFET based buck converter," *IEEE Trans. Ind. Appl.*, vol. 60, no. 5, pp. 7076–7086, Sep./Oct. 2024.
[14] H.-P. Park, M. Kim, and J.-H. Jung, "Spread spectrum technique to reduce EMI emission for an LLC resonant converter using a hybrid modulation method," *IEEE Trans. Power Electron.*, vol. 33, no. 5, pp. 3717–3721, May 2018.
[15] H.-P. Park, M. Kim, and J.-H. Jung, "Spread-spectrum technique employing phase-shift modulation to reduce EM noise for parallel–series LLC resonant converter," *IEEE Trans. Power Electron.*, vol. 34, no. 2, pp. 1026–1031, Feb. 2019.
[16] M. Kim, H.-P. Park, and J.-H. Jung, "Spread spectrum technique for current-fed LLC resonant converter with tight output voltage regulation," in *Proc. 2019 IEEE Energy Convers. Congr. Expo.*, 2019, pp. 6449–6453.
[17] K.-W. Heo, H.-P. Park, and J.-H. Jung, "Spread spectrum modulation to reduce EM noise for LLC resonant converter using partial power processing concept," *IEEE Trans. Power Electron.*, vol. 39, no. 1, pp. 949–960, Jan. 2024.
[18] X. Zhao, D. Jiang, J. Chen, Z. Wang, and Z. Liu, "The impact of periodic variable switching frequency modulation on power transmission in dual-active-bridge converter and an improved scheme," *IEEE Trans. Power Electron.*, vol. 38, no. 11, pp. 13966–13976, Nov. 2023.
[19] K.-W. Heo and J.-H. Jung, "Output voltage compensation using second harmonic ripple in a two-stage converter with spread spectrum modulation," *IEEE Trans. Power Electron.*, vol. 39, no. 12, pp. 16306–16316, Dec. 2024.
[20] H.-P. Park, M. Kim, and J.-H. Jung, "Bidirectional CLLC resonant converter employing PLC capability and em noise reduction technique for small-sized ESS application," *IEEE J. Emerg. Sel. Topics Ind. Electron.*, vol. 2, no. 3, pp. 277–286, Jul. 2021.
[21] S. S. Chakraborty and K. Hatua, "Modeling with beat frequency dynamics and phase-frequency control design for a dual-bridge series resonant converter," *IEEE Trans. Ind. Electron.*, vol. 69, no. 8, pp. 7952–7962, Aug. 2022.
[22] W. Han and L. Corradini, "Wide-range ZVS control technique for bidirectional dual-bridge series-resonant DC–DC converters," *IEEE Trans. Power Electron.*, vol. 34, no. 10, pp. 10256–10269, Oct. 2019.
[23] M. Yaqoob, K. H. Loo, and Y. M. Lai, "A four-degrees-of-freedom modulation strategy for dual-active-bridge series-resonant converter designed for total loss minimization," *IEEE Trans. Power Electron.*, vol. 34, no. 2, pp. 1065–1081, Feb. 2019.
[24] W. Song, M. Zhong, S. Luo, and S. Yang, "Model predictive power control for bidirectional series-resonant isolated DC–DC converters with fast dynamic response in locomotive traction system," *IEEE Trans. Transport. Electrific.*, vol. 6, no. 3, pp. 1326–1337, Sep. 2020.
[25] W. Song, M. Zhong, Y. Deng, S. Yin, and B. Yu, "Model predictive power control for bidirectional series resonant isolated DC–DC converters with steady-state and dynamic performance optimization," *IEEE J. Emerg. Sel. Topics Ind. Electron.*, vol. 3, no. 3, pp. 604–615, Jul. 2022.
[26] S. S. Chakraborty, K. Hatua, and S. Bhattacharya, "A control method to reduce overshoots in high-frequency link current and voltages at load transients of a dual-active-bridge series-resonant converter," *IEEE J. Emerg. Sel. Topics Ind. Electron.*, vol. 4, no. 2, pp. 525–537, Apr. 2023.
[27] K. Ghosh, S. S. Chakraborty, P. Ganesan, and K. Hatua, "A simplified large-signal model-based control for dual active bridge series resonant converter to achieve uniform dynamic response," *IEEE Trans. Power Electron.*, vol. 39, no. 10, pp. 12702–12715, Oct. 2024.
[28] L. Chen, S. Shao, Q. Xiao, L. Tarisciotti, P. W. Wheeler, and T. Dragičević, "Model predictive control for dual-active-bridge converters supplying pulsed power loads in naval DC micro-grids," *IEEE Trans. Power Electron.*, vol. 35, no. 2, pp. 1957–1966, Feb. 2020.
[29] V. Pandey, S. Nayak, K. Hatua, and S. Bhattacharya, "A PCB-incorporated inductor based filter design solution for differential mode noise of 3-phase SiC-MOSFET based VSI," *IEEE Access*, vol. 12, pp. 34958–34972, 2024.
[30] Wurth Electronik, 7448025003 Datasheet WE-CMBNC Common Mode Power Line Choke Nanocrystalline, 2024. Accessed: Jan. 26, 2024. [Online]. Available: https://www.we-online.com/components/products/datasheet/7448025003.pdf
[31] Wurth Electronik, 7448030509 Datasheet WE-CMBNC Common Mode Power Line Choke Nanocrystalline, 2025. Accessed: Jun. 10, 2025. [Online]. Available: https://www.we-online.com/components/products/datasheet/7448030509.pdf

Kousik Ghosh (Student Member, IEEE) was born in West Bengal, India. He received the integrated B.Tech-M.Tech dual degree in electrical engineering from the Department of Electrical Engineering, Indian Institute of Engineering Science and Technology, Shibpur, Howrah, India, in 2020. He is currently working toward the Ph.D. degree in electrical engineering with the Department of Indian Institute of Technology Madras, Chennai, India.

He was a Project Associate for a year in a joint project carried out by Semtronics, U.K., and IIT Madras.

His research interests include advanced control of bidirectional isolated dc–dc converters for various applications and pulsewidth modulation techniques for mitigation of electromagnetic interference.

Vibhav Pandey (Student Member, IEEE) was born in Uttar Pradesh, India. He received the B.Tech degree in electrical engineering from the National Institute of Technology Agartala, Agartala, India, in 2018. He is currently working toward the Ph.D. degree in electrical engineering with the Indian Institute of Technology Madras, Chennai, India.

In 2017, he was an Exchange Student in the final year of B.Tech with the Indian Institute of Technology Madras, Chennai, India. His current research interests include active gate driving techniques and snubber circuit design for SiC MOSFET and EMI/EMC mitigation techniques for SiC-based converters.

Kamalesh Hatua (Member, IEEE) was born in West Bengal, India. He received the Ph.D. degree in electrical engineering from the Indian Institute of Sciences Bangalore, Karnataka, India, in 2011.

He was with BEM Ltd., Mysore, India, and Honeywell Technology Solutions Laboratory, Bangalore, India. He was a Postdoctoral Research Fellow with the FREEDM Center, NCSU, Raleigh, NC, USA. He is currently an Associate Professor with the Department of Electrical Engineering, Indian Institute of Technology Madras, Chennai, India.

His research interests include medium-voltage electric drives, automotive drives, polyphase induction motor drives, active gate driving for SiC switches, solid-state transformer, and design of highly efficient power converters using SiC power switches.